Mesoscale modulation of marine boundary layer water vapor isotopologues during EUREC^{4}A

Joseph Galewsky[1] and Sebastian A. Los[1]

[1]Department of Earth and Planetary Sciences, University of New Mexico, Albuquerque, New Mexico

Correspondence: Joseph Galewsky (galewsky@unm.edu)

Abstract. Shallow cumulus clouds in trade-wind regions remain an important source of uncertainty in climate projections, with competing interpretations of how mesoscale circulations influence boundary layer moisture. We analyze water vapor isotopologue measurements from the EUREC^{4}A campaign to quantify the mesoscale modulation of marine boundary layer humidity and isotopic composition. Surface δD measurements from R/V *Meteor* show a strong sensitivity to mesoscale vertical velocity, substantially exceeding the corresponding response of humidity. Using unstandardized regression slopes, we find that mesoscale ascent partially offsets entrainment-driven isotopic depletion, with approximately 0.7 mm s^{-1} of upward motion required to counteract the isotopic effect of 1 mm s^{-1} of entrainment. The strongest correlations between vertical velocity and both δD ($r \approx 0.52$) and mixing ratio ($r \approx 0.39$) occur within ±200 m of the subcloud layer top, indicating where mesoscale circulations most directly influence near-surface composition. A steady-state flux-form mixed-layer model reproduces the observed asymmetric responses of δD and humidity, providing mechanistic insight into how mesoscale circulations reorganize moisture pathways without producing commensurate changes in total water vapor.

1 Introduction

Shallow cumulus clouds in the trade-wind regions are ubiquitous and exert a cooling influence on the climate, but their response to warming remains uncertain (Bony and Dufresne, 2005). These low clouds have long been recognized as a leading source of spread in climate model projections of global warming (Sherwood et al., 2014). Many climate models predict a positive trade cumulus cloud feedback governed by reductions in cloud fraction near cloud base. In particular, higher-sensitivity models tend to produce more efficient entrainment of dry air from aloft, which depletes low-level humidity and erodes cloud cover (Sherwood et al., 2014). This hypothesized mixing–desiccation mechanism posits that vigorous shallow convective mixing dries the lower troposphere and dissipates clouds, thereby amplifying surface warming as a positive low-cloud feedback.

Recent observations, however, challenge this picture. In early 2020, the EUREC^{4}A field campaign (Elucidating the Role of Clouds–Circulation Coupling in Climate) was conducted near Barbados with a network of research aircraft, ships, and ground stations to study trade-wind cumulus and their environment (Bony et al., 2017; Stevens et al., 2021). Analyses of EUREC^{4}A data revealed shallow mesoscale circulations on scales of roughly 100–200 km that organize convection and concentrate moisture in the trades (George et al., 2023). Consistent with this, periods of stronger mesoscale ascent did not lead to a drier subcloud layer (SCL) or reduced cloudiness, contrary to the mixing–desiccation expectation (Vogel et al., 2022). Instead, the observations suggest that mesoscale cloud–circulation coupling can maintain humidity, implying that factors beyond one-dimensional entrainment, such as horizontal convergence and large-scale vertical motion, significantly influence low-level moisture and cloud cover. Nevertheless, disentangling the contributions of these processes, for example separating the effects of shallow convective detrainment from those of large-scale subsidence, remains challenging with conventional measurements alone. Standard thermodynamic observations cannot easily attribute moisture variability to specific physical processes, leaving an important gap in process-level understanding of the trade cumulus regime.

Stable water isotopologues offer a way to fill this gap. The ratios of heavy to light water isotopologues in vapor, such as $H_2^{18}O/H_2^{16}O$ or HDO/H_2O, commonly reported as $\delta^{18}O$ and δD, are sensitive to the cumulative phase-change history of an air mass (Galewsky et al., 2016). Condensation and rainout preferentially remove heavy isotopes, so air that has undergone extensive convective uplift and precipitation is left isotopically depleted in heavy molecules relative to ocean water. In contrast, addition of moisture by evaporation from the warm ocean surface, or by mixing with unsaturated air from below, enriches the vapor in heavy isotopes. Thus, water vapor isotopic measurements can serve as tracers of moisture origin and transport. They enable us to distinguish between air masses that have experienced different water-cycle processes and to test hypotheses about what controls an air mass's humidity and cloud-forming potential. Past studies have demonstrated that isotopic variations can be used to identify moisture sources and quantify mixing between atmospheric layers, processes that are largely indistinguishable in bulk humidity alone (Risi et al., 2019; Galewsky et al., 2016).

EUREC^{4}A included a coordinated initiative (EUREC^{4}A-iso) to deploy an extensive network of water vapor isotope analyzers across multiple platforms (Bailey et al., 2023). Seven laser-based instruments, sampling at up to 0.5 Hz, were operated on two research aircraft, three ships, and at the Barbados Cloud Observatory during the campaign. This data set provides the high-resolution, multi-platform coverage needed to close regional moisture budgets and evaluate model simulations of moist processes. Here, we use the EUREC^{4}A water vapor isotopic measurements from the R/V Meteor to bridge the gap between documented mesoscale circulation effects and their impacts on the marine boundary layer moisture budget. Specifically, we use the stable isotope signatures to directly track shallow convective mixing and its influence on lower-tropospheric moisture in the trade-wind regime.

2 Data

EUREC^{4}A comprised about 5 weeks of measurements in the downstream winter trades of the North Atlantic, eastward and southeastward of Barbados. The campaign deployed an extensive observational network to characterize processes operating across scales from micrometers to hundreds of kilometers. The measurements included 2500 atmospheric soundings to quantify mesoscale and larger-scale atmospheric properties, approximately 400 flight hours by four research aircraft, operations from four research vessels, and continuous observations from a ground-based cloud observatory. Additional platforms included autonomous systems that collected nearly 10,000 upper-ocean profiles, continuous atmospheric boundary layer measurements, air-sea interface observations, water vapor isotopologue measurements across multiple platforms, coordinated satellite observations, and support from high-resolution numerical weather and climate models.

2.1 Upper Air Data

The dropsonde measurements were conducted using two research aircraft: the High Altitude and Long Range Research Aircraft (HALO) (Konow et al., 2021) and the NOAA WP-3D Orion (P-3) (Pincus et al., 2021). The primary scientific motivation for these measurements was to characterize the area-averaged kinematic environment of trade-wind cumulus cloud fields and to quantify area-averaged vertical motion in the marine boundary layer. The cornerstone of the measurement strategy was the EUREC^{4}A-circle (Figure 1), a standardized circular flight pattern designed to enable accurate estimates of properties including divergence, vorticity, and vertical velocity. This approach, adapted from Lenschow et al. (1999, 2007) and Bony and Stevens (2019), exploits the assumption that atmospheric variations at the mesoscale can be approximated as linear in horizontal space over the scale of a single aircraft circle.

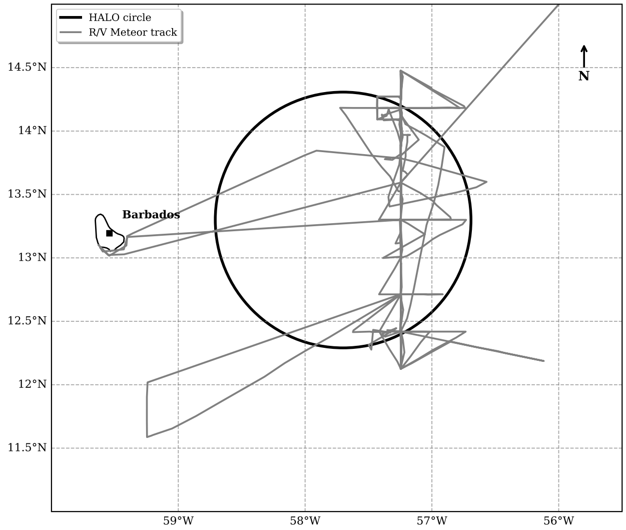

Figure 1. Map of the EUREC^{4}A study area showing a representative EUREC^{4}A circle pattern and the R/V Meteor ship track. The circle (black) represents one of the 222 km diameter flight patterns used for dropsonde deployment to measure mesoscale circulation. The ship track (gray) shows the path of R/V Meteor during the January–February 2020 field campaign.

The EUREC^{4}A-circle was centered at 13.30°N, 57.72°W with a diameter of approximately 222 km. Each circle flight pattern deployed 12 dropsondes at regular intervals around the circumference, with launches separated by approximately 5 minutes corresponding to the aircraft's 60-minute circuit time. This systematic sampling enables estimation of horizontal gradients through regression analysis, from which mesoscale circulation properties can be derived.

A total of 85 EUREC^{4}A-circles were flown during the campaign (71 by HALO and 14 by the P-3), providing unbiased sampling across meteorological conditions. All flights operated from Bridgetown, Barbados, with HALO operating at altitudes between 10.0–10.5 km, while the P-3 typically flew at lower altitudes near 7.5 km as part of the ATOMIC component of the campaign (Pincus et al., 2021). A total of 1216 Vaisala RD-41 dropsondes were launched (896 from HALO and 320 from the P-3), each containing pressure, temperature, and humidity sensors sampling at 2 Hz, along with GPS receivers providing wind measurements at 4 Hz. The measurements are archived in the JOANNE dataset (George et al., 2021), from which we use the Level 4 circle-averaged products containing mesoscale diagnostics derived through regression analysis of the 12-sonde circle patterns. These products include horizontal gradients of atmospheric variables and derived quantities such as divergence, vorticity, horizontal divergence of wind velocity, and vertical velocity, with associated uncertainty estimates from the regression fitting.

The subcloud layer height h used here was first presented in Vogel et al. (2022) and is determined using a temperature-based threshold method (Albright et al., 2022). Specifically, h is defined as the height where the virtual potential temperature θ_v first exceeds its density-weighted mean value (computed from 100 m up to h) by a fixed threshold $\epsilon = 0.2$ K (Vogel et al., 2022). This approach follows established methodology for identifying the top of the well-mixed subcloud layer (Touzé-Peiffer et al., 2022). The method accounts for the finite thickness of the transition layer separating the mixed layer from the cloud layer above (Albright et al., 2022). This transition layer, approximately 150 m thick, complicates the application of classical mixed-layer theory which assumes an infinitesimally thin inversion.

The entrainment rate E is computed using a modified flux-jump model (Albright et al., 2022; Vogel et al., 2022) that extends the classical approach of Lilly (1968) and Stull (1976). The entrainment rate represents the deepening of h due to small-scale mixing at the subcloud layer top. This approach differs from the zero-order jump models that assume instantaneous transitions (Lilly, 1968) by accounting for the finite depth of the entrainment zone, providing a more realistic representation of the actual atmospheric structure observed during EUREC^{4}A. Note that throughout this study, E refers only to entrainment from the cloudy layer (CL) into the subcloud layer (SCL). It does not include exchange between the CL and the free troposphere (FT). Here, E represents a diagnostically inferred entrainment tendency at the cloud–subcloud interface; negative values indicate periods of interface descent or weak detrainment rather than physically negative turbulent entrainment. Across the matched circles, the average entrainment rate, E = $18.8 \pm 6.9\ \mathrm{mm\ s^{-1}}$ and the average subloud layer height is $h = 0.69 \pm 0.10\ \mathrm{km}$.

2.2 Isotopic and Surface Data

Water vapor isotope measurements aboard the R/V Meteor were obtained using a Picarro L2130-i cavity ring-down spectrometer (CRDS) operating at 1 Hz resolution from January 18 to February 22, 2020. The analyzer was housed in the Air-Chemistry Laboratory at ∼20.3 m above sea level, sampling ambient air through a 5 m long, 4.6 mm ID PTFE inlet line heated to 45°C and insulated with polyethylene foam. The inlet was housed in a downward-facing funnel to minimize contamination from rainwater and sea spray, and included a 0.2 μm PTFE aerosol filter. Flow was controlled by the CRDS system at approximately 0.03 slpm, resulting in a time delay of >2 minutes from intake to analyzer. Daily calibration checks were performed using four liquid water standards spanning δ^{18}O values from -20.97 to -2.79‰ and δD values from -158.13 to -13.12‰, delivered in gas phase using a Picarro Standards Delivery Module. Prior to normalization, isotopic observations were corrected for small humidity-dependent biases of up to 0.24‰ in δ^{18}O and 0.36‰ in δD. Total uncertainties were estimated at 0.29‰ for δ^{18}O and 1.24‰ for δD by summing in quadrature the uncertainties associated with liquid standards, humidity-dependence correction, calibration measurement precision, and temporal drift over the campaign. Further details on the isotopic data collection program can be found in Bailey et al. (2023).

Near-surface relative humidity data were obtained from temperature and dew point measurements made at 29 m above the sea surface on the Meteor's mast. SST was measured at 2.3 m depth with matching port and starboard sensors.

3 Results

Figure 2 presents the full time series of surface water vapor measurements, relative humidity (RH) and sea surface temperature (SST) measured from the R/V *Meteor* during EUREC^{4}A. The dataset exhibits relatively low variability across all measured parameters, reflecting the stable trade wind conditions that characterized the campaign period. Water vapor mixing ratios varied with a standard deviation of 0.832 g kg^{-1} around a mean of 15.1 g kg^{-1}, while δD showed a standard deviation of 1.94‰ around a mean of -70.6‰. Surface meteorological variability was also limited, with relative humidity varying by 4.6% around a mean of 71.6% and sea surface temperatures showing little variation (standard deviation 0.23°C) around 27.3°C. The measurement uncertainty for 2-hour averaged isotope data (1.24‰ for δD) represents approximately 65% of the observed natural variability, limiting our ability to detect weak atmospheric signals. Consequently, our analysis focuses on the strongest and most robust correlations that exceed this measurement noise threshold.

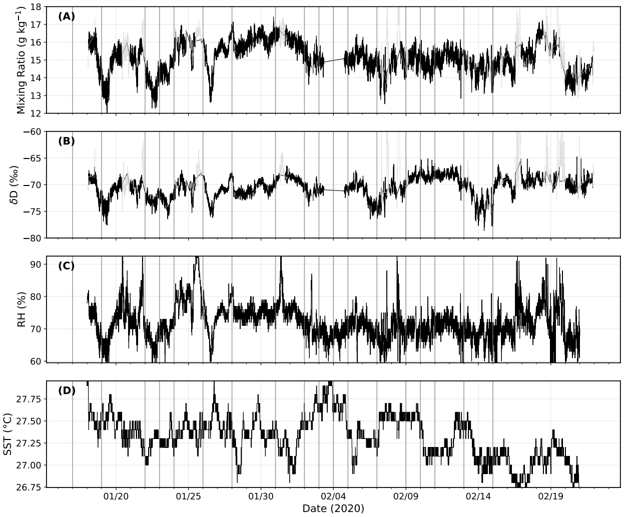

Figure 2. Time series of surface measurements from R/V *Meteor* during EUREC^{4}A, January 18–February 22, 2020. (A) Water vapor mixing ratio from Picarro L2130-i cavity ring-down spectrometer at 1-minute resolution. (B) Deuterium isotope ratio (δD) from the same instrument. (C) Relative humidity from shipboard meteorological sensors. (D) Sea surface temperature. Black lines indicate quality-controlled data; pale gray points show measurements flagged during quality control. Gray vertical lines mark days with HALO/P3 aircraft circle flights from the JOANNE dropsonde dataset.

Figure 3 shows the vertical correlation structure between dropsonde-derived vertical velocity and surface isotopic composition (δD) and mixing ratio as a function of altitude relative to the top of the subcloud layer. Both δD (solid line) and mixing ratio (dashed line) exhibit their strongest correlations just below this boundary. The isotopic signal shows peak correlation ($r \approx 0.52$) about 100 meters below the top of the SCL, while humidity correlations reach maximum strength ($r \approx 0.39$) about 100 meters lower within the SCL.

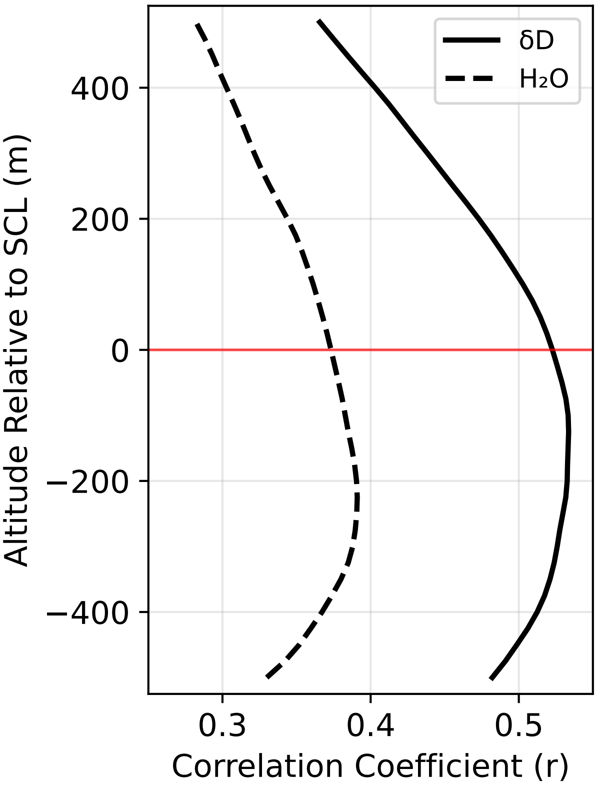

Figure 3. Vertical velocity correlation profiles with isotopic composition and humidity near subcloud layer height. Correlation coefficients between vertical velocity (W) and water vapor δ D (solid black line) and water vapor mixing ratio (dashed black line) are shown as functions of altitude relative to the top of the subcloud layer (SCL, red horizontal line at 0 m). The analysis spans ±500 m around the top of the SCL, which is defined as the height where virtual potential temperature first exceeds its density-weighted mean from 100 m by 0.2 K. Both variables show peak correlations within the subcloud layer, with δD exhibiting stronger coupling to vertical motion than humidity.

Figure 4 shows (a) entrainment rate E (light blue) and vertical velocity W from 100 m below the top of the SCL (dark blue), both in mm s^{-1}; (b) surface δD in ‰; and (c) water vapor mixing ratio in g kg^{-1}. Each point represents a 2-hour average centered on a HALO/P3 circle time. The time series shows coherent variability across all of these parameters. Periods of enhanced entrainment (positive E values) consistently coincide with more negative δD and lower mixing ratio, as seen most clearly around January 26. Conversely, periods of weak entrainment or stronger mesoscale ascent (negative E, positive

W) correspond to less negative δD and higher mixing ratios, evident around January 24 and February 1. Entrainment brings dry, isotopically depleted air from above the SCL into the surface layer, reducing humidity and driving δD toward more negative values (and overwhelming any potential increase in surface evaporation due to associated winds). Periods of reduced entrainment or mesoscale upward motion allow the boundary layer to maintain higher humidity and preserve the enriched isotopic signatures characteristic of ocean evaporation.

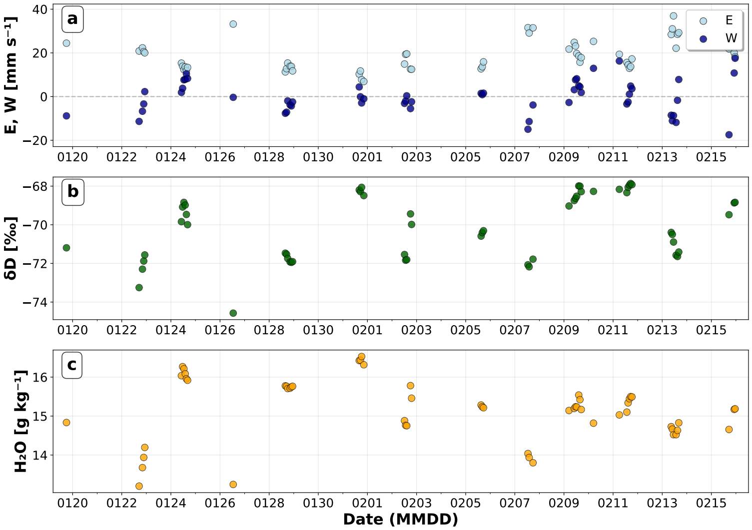

Figure 4. Time series of atmospheric variables during the EUREC^{4}A campaign. (a) Entrainment rate E (light blue) and mesoscale vertical velocity W from 100 m below the top of the SCL (dark blue) in mm s^{-1}, showing the competing effects of horizontal dry air mixing and convective vertical motion. The dashed gray line indicates zero. (b) Surface boundary layer δD in ‰, measured by ship-based Picarro analyzer. (c) Water vapor mixing ratio H_2O in g kg^{-1} from matched HALO/P3-Picarro observations. All data points represent 2-hour averaged values spatially matched within HALO/P3 flight circles. The time axis shows dates in MMDD format during January-February 2020. Data demonstrate the temporal evolution of entrainment-convection competition and its effects on boundary layer moisture and isotope signatures.

This structure is further illustrated in Figure 5, which shows the relationship between vertical velocity W (x-axis) and entrainment rate E (y-axis), with points colored by surface δD and sized according to water vapor mixing ratio. The scatter plot reveals a systematic organization of boundary layer states across the E–W parameter space. Points in the upper-left quadrant (negative W, high E) correspond to conditions of strong entrainment combined with mesoscale downdrafts and are characterized by more negative δD values and lower mixing ratios. Points toward the lower right (positive W, low E) indicate periods of weaker entrainment and mesoscale ascent, which are associated with less negative δD values and modestly higher humidity.

A linear regression across all matched circles ($n = 56$) yields

$$E = -0.25(\pm 0.24)\,W + 18.6, \tag{1}$$

with a statistically significant negative slope ($p = 0.044$, 95% confidence interval $[-0.49, -0.01]$), indicating that entrainment and vertical velocity are weakly but systematically anticorrelated. Although this relationship exhibits substantial scatter, it demonstrates that E and W are not independent but instead span a continuum of boundary layer mixing states.

Consistent with this organization, the δD color gradient transitions from more depleted values under high-E, negative-W conditions toward more enriched values under low-E, positive-W conditions. Marker sizes increase along this same trajectory, indicating that periods of reduced entrainment and mesoscale ascent coincide with isotopic enrichment and enhanced humidity.

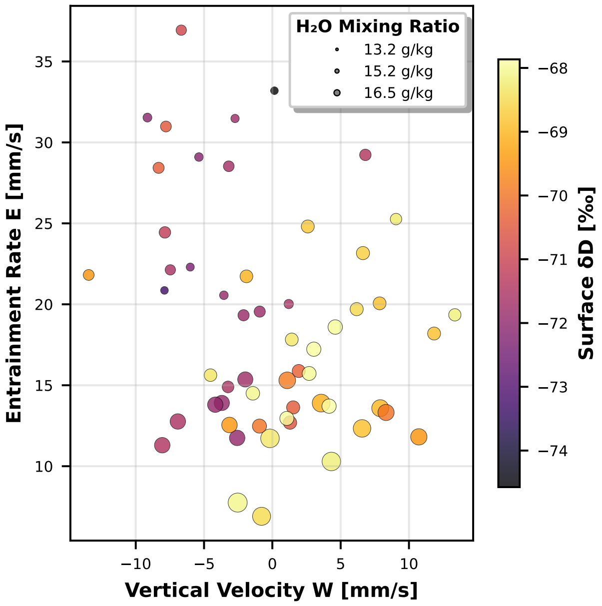

Figure 5. Relationships between vertical velocity (W), entrainment rate (E), water vapor mixing ratio, and water vapor δD during EUREC^{4}A. Scatter plot shows W extracted at altitude of maximum correlation from Figure 4 (567.7 m above the sea surface) versus entrainment rate E, with circle size proportional to water vapor mixing ratio (H_2O) and color representing surface δD. Data points represent individual dropsonde circles matched with ship-based isotope measurements.

A more quantitative understanding of these relations is illustrated in Figs. 6 and 7. Figure 6 shows the joint dependence of isotopic composition and humidity on both entrainment and vertical velocity. Panel ()A) shows δD values across the E-W parameter space, with contour lines representing predictions from a joint linear regression model that includes both E and W as predictors. The isotopic field exhibits a systematic gradient from depleted values (δD $\approx$ -73‰) at high entrainment rates and negative vertical velocities to enriched values (δD $\approx$ -68‰) at low entrainment and positive vertical velocities. Panel (B) shows the corresponding humidity field, where water vapor mixing ratios decrease from approximately 16.5 g kg^{-1} at low E and high W to 13.5 g kg^{-1} at high E and low W. To quantify these relationships, we performed a joint multilinear regression for both variables. The regression for δD yields $\delta D = -0.071E + 0.100W - 68.74$ ($R^2 = 0.357$), where both predictors are statistically significant at the 5% level ($p \approx 0.013$ for E and $p \approx 0.00027$ for W), with a residual mean absolute error (MAE) of 1.15‰

and an RMSE of 1.33‰. For specific humidity, the regression yields $H_2O = -0.083E + 0.019W + 16.72$ ($R^2 = 0.633$), with coefficients that are also significant ($p \approx 2.5 \times 10^{-11}$ for E and $p \approx 0.040$ for W) and a residual MAE of 0.365 g kg^{-1} and RMSE of 0.472 g kg^{-1}. These results quantify the "diagonal" structure seen in the parameter space, demonstrating that both predictors are statistically significant, with a moderate fit for δD and a stronger fit for H_2O. The orientation of the contours in both panels further confirms that δD is more sensitive to W than the total mixing ratio, which is more sensitive to entrainment.

In interpreting these results, we note that E and W are not independent predictors; in our dataset, they exhibit a modest negative correlation ($r \approx -0.27$). However, the joint multilinear regression framework used here specifically accounts for this covariance. The reported MLR coefficients represent partial slopes, quantifying the independent impact of each variable while holding the other constant. Consequently, the distinct sensitivities observed for δD and humidity are robust signatures of the physical processes driving each variable, rather than artifacts of the correlation between entrainment and vertical motion.

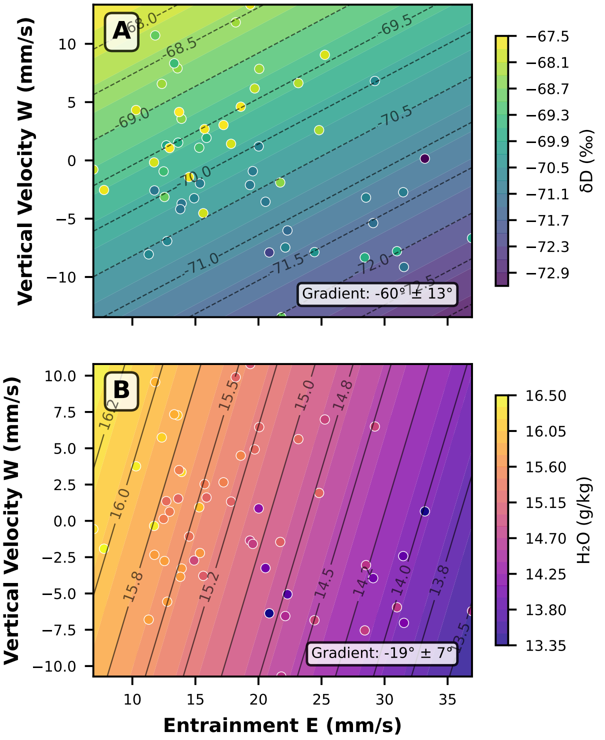

Figure 6. Joint entrainment-vertical velocity dependencies in isotopic composition and humidity fields. (A) Contour plot showing water vapor δ D as a function of entrainment rate E and vertical velocity W, with observations overlaid as colored points. Contour lines represent predictions from the joint E-W regression model. (B) Water vapor mixing ratio (H2O) dependencies on the same E-W parameter space, using a different color scheme to distinguish variables.

Figure 7 further quantifies the counteraction effect of mesoscale vertical velocity (W) on entrainment (E) through residual analysis. This approach first removes the linear effect of entrainment alone, then examines how vertical velocity correlates with the remaining variance. Using the full dataset ($n = 56$), the standardized regression coefficients for δD are $\beta_E = -0.49$ and $\beta_W = +0.74$. For humidity, the standardized coefficients are $\beta_E = -0.57$ and $\beta_W = +0.14$. These coefficients are obtained from the joint regression and do not assume independence between E and W.

The δD residuals (Panel A) exhibit a strong positive correlation with W ($r = 0.464$), indicating that upward motion systematically counteracts entrainment-driven isotopic depletion. We define a counteraction efficiency metric as the ratio of the absolute values of the standardized regression coefficients,

$$\eta = \left|\frac{\beta_W}{\beta_E}\right|, \tag{2}$$

which quantifies the relative statistical influence of mesoscale ascent and entrainment in units of standard deviations. For δD, this yields $\eta_{\delta D} \approx 1.5$, whereas for humidity the corresponding value is much smaller, $\eta_q \approx 0.25$.

Because this metric is based on standardized coefficients, it does not represent cancellation in physical units (mm s^{-1}), but instead compares the sensitivity of each variable to variability in the two predictors. Physical cancellation in mm s^{-1} can instead be assessed using the unstandardized regression slopes. From the fitted relationship

$$\delta D = -0.071\,E + 0.100\,W - 68.74, \tag{3}$$

we find that approximately 0.7 mm s^{-1} of mesoscale ascent is required to offset the isotopic impact of 1 mm s^{-1} of entrainment.

The counteraction efficiency for δD indicates that mesoscale processes exert a stronger relative influence on isotopic variability than entrainment alone, whereas the lower efficiency for humidity reflects the comparatively weak role of vertical motion in setting boundary-layer water vapor concentrations. Although these relationships exceed the noise threshold identified earlier, measurement uncertainty constitutes a large fraction of the observed δD variance. As a result, the precise values of the regression slopes and efficiencies should be interpreted cautiously, even though the qualitative contrast between isotopic and humidity responses is robust.

These results show that mesoscale circulations significantly modulate the entrainment-driven changes in boundary layer humidity and composition, consistent with the findings of Vogel et al. (2022) and George et al. (2023). The isotopic measurements provide quantitative constraints on the relative importance of these competing processes, with mesoscale vertical motions capable of fully offsetting or even reversing entrainment effects on boundary layer moisture δD.

3.1 Flux-Form Mixed-Layer Model

To identify the physical mechanisms responsible for the asymmetric responses of δD and q, we applied the flux-form mixed-layer model described in Appendix A. Unlike simpler mixing definitions that treat the subcloud layer (SCL) as a passive reservoir, this model explicitly resolves the competing isotopic fluxes driven by surface evaporation, entrainment mixing, and active hydrometeor exchange.

The model's moisture budget is determined by the balance between two primary processes: surface evaporation, which moistens and isotopically enriches the boundary layer, and entrainment of air from the cloudy layer, which dries and isotopically depletes it. We formulate the surface flux using a physically consistent Craig–Gordon approximation that accounts for the

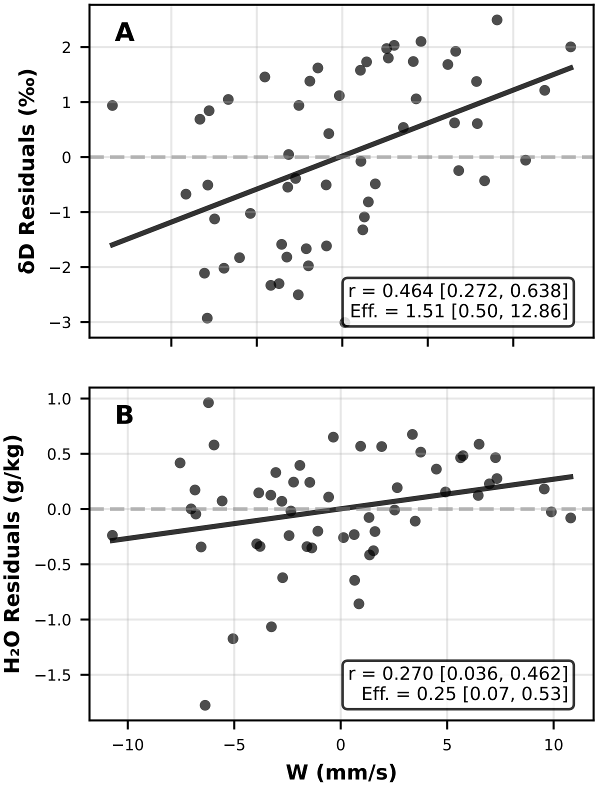

Figure 7. Residual analysis of vertical velocity counteraction effects on isotopic composition and humidity. (A) ΔD residuals after removing entrainment-only effects plotted against vertical velocity W at optimal altitude. Points show individual HALO/P3 circle observations, with the regression line indicating the pure counteraction effect of W. The correlation coefficient (r) and counteraction efficiency (Eff.) quantify how effectively vertical motion counteracts entrainment-driven isotopic depletion. (B) Water vapor mixing ratio (H2O) residuals after removing entrainment-only effects plotted against vertical velocity W.

cancellation of humidity singularities in the mass and isotope budgets (see Appendix A), ensuring that the model respects the mass balance constraints of the system.

However, standard mixing dynamics alone cannot reproduce the observed slope separation between δD and humidity. In a “passive” mixing regime, where the SCL interacts only with the ocean surface and the dry free troposphere, isotopic composition and humidity are tightly coupled, resulting in δD and q contours that are nearly parallel. To capture the observed orthogonality (Fig. 8), the model must account for the active processing of water vapor by liquid water within the trade-wind layer.

We therefore introduce a hydrometeor exchange mechanism that represents the interaction between subcloud vapor and falling rain or drizzle droplets. This process is physically justified by the ubiquity of warm rain in the trade-wind regime; EUREC^{4}A observations confirm that rain evaporation is a frequent and significant contributor to the subcloud moisture budget, often manifesting as cold pools (Touzé-Peiffer et al., 2022; Radtke et al., 2022). Previous modeling studies of trade cumulus have similarly established that rain evaporation is a critical term for closing the isotopic budget, as falling droplets transport heavy isotopes from the cloud layer back into the subcloud environment (Risi et al., 2020).

In our model, this exchange is parameterized as a relaxation toward an enriched hydrometeor equilibrium, with an efficiency that scales with mesoscale vertical velocity (W). Physically, this dependency reflects the dynamical nature of the cloud field: mesoscale ascent organizes convection and increases cloud fraction (George et al., 2023), thereby generating the precipitation flux necessary to drive isotopic exchange. During periods of ascent, this "recharging" mechanism counteracts the depletion caused by entrainment, effectively buffering the isotopic composition of the boundary layer even as entrainment continues to regulate the bulk humidity.

Figure 8 presents the modeled equilibrium state for humidity (dashed blue contours) and δD (solid black contours) across the entrainment–vertical velocity (E–W) phase space. The model successfully reproduces the nearly orthogonal structure observed in the campaign data (compare to Figure 6). The modeled humidity contours are steep (slope $\approx 77°$), indicating that q_{BL} is primarily controlled by the entrainment rate E and is relatively insensitive to W. In contrast, the modeled δD contours are much flatter (slope $\approx 35°$), indicating an important sensitivity to vertical velocity. This successful reproduction of the E–W phase space provides evidence that the trade-wind boundary layer cannot be treated as a simple two-component mixing system; rather, its composition is actively shaped by phase-change physics modulated by mesoscale circulations.

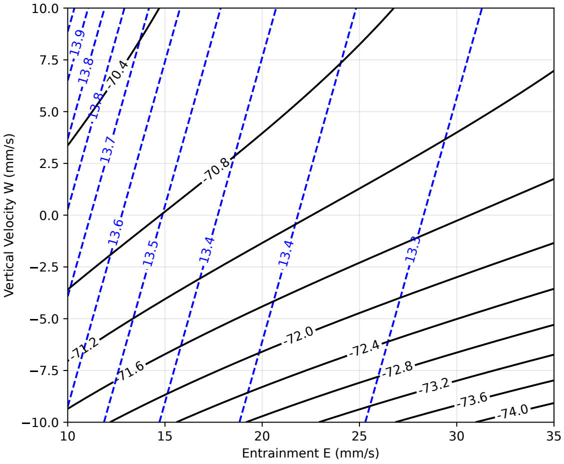

Figure 8. Equilibrium solution of the strictly consistent flux-form mixed-layer model (v23) across the entrainment (E) and vertical velocity (W) parameter space. Dashed blue lines show specific humidity (q_{BL}), which is dominated by entrainment (steep contours). Solid black lines show isotopic composition (δD), which is strongly modulated by vertical velocity (flatter contours). The divergence of these slopes (approx. $77°$ vs. $35°$) reproduces the first-order effects observed in the EUREC^{4}A data, showing how active isotopic exchange during ascent is required to explain the observations.

4 Discussion

Our analysis shows that mesoscale vertical motions in the trade-wind regime modulate the marine boundary layer through a partial counteraction of entrainment-driven drying. Water vapor isotopologues reveal this modulation with greater sensitivity than humidity alone, yielding an asymmetric response: δD varies more strongly with mesoscale vertical velocity than does the total mixing ratio. A flux-form mixed-layer model reproduces this behavior and indicates that, under the observed conditions, δD responds about six times more strongly than humidity to mesoscale vertical motion. Together, these results show that mesoscale circulations reorganize boundary layer moisture in ways that are weakly expressed in humidity but strongly expressed in isotopic composition.

Throughout this study, E refers exclusively to entrainment from the cloudy layer (CL) into the subcloud layer (SCL) and does not include exchange between the CL and the free troposphere (FT). Negative values of E are interpreted as reflecting reduced or reversed apparent entrainment tendencies associated with mesoscale subsidence or interface lowering, rather than literal negative turbulent entrainment fluxes.

4.1 Connection to mesoscale overturning circulations and mixing–desiccation processes

These findings provide observational and mechanistic context for the shallow mesoscale overturning circulations (SMOCs) identified by George et al. (2023) and the counteraction mechanism proposed by Vogel et al. (2022). Vogel et al. (2022) demonstrated that mesoscale vertical motions counteract entrainment-driven drying, refuting the mixing–desiccation hypothesis of Sherwood et al. (2014) by showing that stronger mixing does not necessarily lead to cloud-base desiccation. George et al. (2023) provided direct observational evidence of SMOCs, documenting robust divergence dipoles between the subcloud and cloud layers and showing that convergence branches reduce entrainment efficiency and amplify moisture variance near cloud base.

Our analysis extends these studies by localizing the coupling mechanisms in the vertical. The strongest correlations between vertical velocity and both δD and humidity occur just below the subcloud layer top, identifying where mesoscale circulations most directly influence near-surface composition. This vertical localization sharpens the physical picture of SMOC-driven moisture regulation and demonstrates that mesoscale ascent maintains enriched isotopic signatures characteristic of oceanic evaporation, while descent enhances the influence of entrained cloudy-layer air. The resulting isotopic contrast between ascending and descending branches exceeds the corresponding humidity contrast.

4.2 Why isotopes respond more strongly than humidity

The pronounced isotopic sensitivity arises because δD responds to moisture source and processing history, whereas humidity is constrained by near-instantaneous mass balance. Mesoscale ascent modifies entrainment, cloud residence time, and interaction with condensate in ways that strongly affect isotopic composition but only weakly alter total water vapor. As a result, mesoscale circulations reorganize moisture pathways and phase-change histories without producing commensurate changes in mixing ratio.

This asymmetry is evident in the joint entrainment–vertical velocity (E–W) space, where δD exhibits a strong diagonal organization analogous to the SMOC moisture anomaly structure described by George et al. (2023), but with larger amplitude. While both δD and humidity respond to entrainment, mesoscale ascent produces large isotopic enrichment with only modest moistening. Isotopic tracers therefore expose compensation mechanisms that remain largely hidden in humidity alone.

4.3 Relation to existing isotope frameworks

Our results extend existing theoretical and observational frameworks for marine boundary layer isotopic composition. The MBL-mix model of Benetti et al. (2018) successfully reproduces isotopic variability through surface evaporation and mixing with isotopically depleted air aloft. Our analysis shows that mesoscale vertical motions introduce an additional dynamical modulation of these processes, altering the effective contribution of cloudy-layer air on timescales shorter than those typically considered in two-endmember frameworks.

Similarly, the asymmetric isotopic response we document is consistent with the processes outlined by Galewsky et al. (2022), who showed that water vapor isotopologues provide sensitivity to boundary layer mixing and decoupling processes in stratocumulus regimes that is not evident from humidity alone. Our EUREC^{4}A observations demonstrate that this sensitivity extends to the trade cumulus regime and is expressed through mesoscale overturning circulations rather than solely through boundary layer decoupling. The vertical localization observed here provides a mechanistic link between surface isotopic signatures and mesoscale circulation patterns that transport locally evaporated but differentially processed vapor within the boundary layer.

Our findings also complement the analysis of Risi et al. (2019), who emphasized the role of local mixing processes in controlling isotopic variability. We show that this mixing is dynamically modulated rather than passive: mesoscale vertical motion alters the isotopic character of the entrained air itself by redistributing vapor that has undergone different degrees of cloud processing. During active mesoscale periods, the boundary layer cannot be treated as a simple two-endmember system.

4.4 Broader implications and limitations

The strong isotopic sensitivity to mesoscale vertical motion provides an observational constraint on boundary layer coupling that is not available from humidity alone. Large-eddy simulations of shallow convection often exhibit weak mesoscale signals in subcloud-layer humidity due to efficient turbulent mixing (Bretherton and Blossey, 2017; Janssens et al., 2023). Our isotopic observations demonstrate that mesoscale dynamics nevertheless leave a clear imprint on near-surface composition, indicating that δD is a sensitive tracer of mesoscale–surface coupling even when humidity anomalies are muted.

While our analysis focuses on mesoscale circulations, cold pools and precipitation also influence boundary layer structure during EUREC^{4}A (Touzé-Peiffer et al., 2022; Radtke et al., 2022). The strongest isotopic–vertical velocity correlations occur near 500–600 m, generally above the shallowest layers most strongly affected by cold-pool outflows. This suggests that the isotopic signal primarily reflects deeper mesoscale overturning rather than near-surface cold-pool dynamics, though future work explicitly incorporating cold-pool diagnostics would help further separate these influences.

Overall, our results show that the marine boundary layer isotopic composition emerges from the combined effects of surface evaporation, entrainment mixing, cloud processing, and mesoscale circulation modulation. These processes are not independent: mesoscale vertical motion dynamically reshapes mixing pathways without producing proportional changes in humidity. This asymmetric response highlights the value of isotopic measurements as probes of mesoscale dynamics and provides a framework for incorporating isotope constraints into representations of shallow convection and cloud feedbacks.

5 Conclusions

The goal of this study was to quantify how mesoscale vertical motions modulate marine boundary layer moisture and isotopic composition in the trade-wind regime, and to test interpretations of the mixing–desiccation hypothesis using water vapor isotopologue observations from EUREC^{4}A.

Our main findings are as follows:

1. Water vapor δD and mixing ratio exhibit distinct sensitivities to mesoscale circulation. While humidity variability is primarily controlled by entrainment, δD is more strongly modulated by mesoscale vertical velocity, demonstrating that isotopic composition encodes mesoscale dynamics more clearly than humidity alone.
2. Using standardized regression coefficients, we find that mesoscale vertical velocity exerts a stronger relative influence on δD than entrainment does, with a counteraction efficiency of $\eta_{\delta D} \approx 1.5$. In contrast, the corresponding efficiency for humidity is much smaller ($\eta_q \approx 0.25$), highlighting a pronounced asymmetry in the response of isotopic composition and total moisture to mesoscale forcing.
3. The strongest correlations between vertical velocity and both δD ($r \approx 0.52$) and mixing ratio ($r \approx 0.39$) occur within approximately ±200 m of the subcloud layer top, identifying the vertical region where mesoscale circulations most directly influence near-surface composition.
4. Periods of enhanced entrainment are consistently associated with more negative δD values and lower mixing ratios, whereas periods of mesoscale ascent correspond to less negative δD and modest moistening. Together, these relationships reveal a systematic organization of boundary layer states across entrainment–vertical velocity space, consistent with shallow mesoscale overturning circulations.
5. A steady-state, flux-form mixed-layer model reproduces the observed asymmetric responses of δD and humidity without ad hoc tuning. The model shows that isotopic composition is intrinsically more sensitive than humidity to changes in the relative contributions of surface and cloudy-layer sources, providing mechanistic closure for the observed counteraction between entrainment and mesoscale ascent.

Although the natural variability of δD during the campaign is modest and quantitative sensitivities should therefore be interpreted cautiously, the convergence of observational diagnostics and model behavior supports a robust qualitative conclusion: water vapor isotopologues provide a sensitive tracer of mesoscale circulations in the trade-wind boundary layer that is not accessible from humidity measurements alone. These results refine interpretations of the mixing–desiccation hypothesis by showing that mesoscale vertical motions reorganize moisture pathways and source contributions without producing commensurate changes in total water vapor, underscoring the value of isotopic constraints for understanding boundary layer dynamics and cloud–circulation coupling.

Data availability. EUREC^{4}A water vapor isotope data from R/V Meteor and HALO/P3 dropsonde data from the JOANNE dataset are publicly available through the EUREC^{4}A data portal at https://eurec4a.eu/data.

Appendix A: Flux-Form Mixed-Layer Model Formulation

A1 Model Framework

We employ a steady-state, flux-form mixed-layer model to resolve the budget of specific humidity (q_{BL}) and isotopic ratio (R_{BL}) within the subcloud layer (SCL). The model treats the SCL as a well-mixed slab of depth h that interacts with three reservoirs: the ocean surface, the free troposphere/cloud layer above, and a hydrometeor reservoir (rain/cloud droplets) driven by mesoscale ascent. Note that we use the subscript ’BL’ to denote bulk properties of the well-mixed SCL.

A2 Moisture Budget

The steady-state mass budget for specific humidity q_{BL} is defined by the balance between surface evaporation and entrainment drying:

$$0 = F_E + F_{\mathrm{ent}}, \tag{A1}$$

where F_E is the surface evaporative mass flux and F_{ent} is the net entrainment flux. We parameterize the surface flux as a relaxation toward saturation:

$$F_E = \lambda(q_s - q_{\mathrm{BL}}), \tag{A2}$$

where λ (s^{-1}) is a surface coupling timescale and q_s is the saturation specific humidity at sea surface temperature (SST) and pressure. Note that by definition $q_{\mathrm{BL}} = \mathcal{H} q_s$, where $\mathcal{H}$ is the relative humidity (normalized to 1). Therefore, Eq. (A2) can be written as $F_E = \lambda q_s(1-\mathcal{H})$.

The entrainment flux is parameterized as:

$$F_{\mathrm{ent}} = \varepsilon_{\mathrm{eff}}(q_{\mathrm{FT}} - q_{\mathrm{BL}}), \tag{A3}$$

where q_{FT} is the humidity of the overlying cloudy layer. To represent the modulation of boundary layer ventilation by mesoscale circulations, we define an effective entrainment rate $\varepsilon_{\mathrm{eff}}$:

$$\varepsilon_{\mathrm{eff}} = \max\left(\frac{E - \gamma W}{h}, 0\right). \tag{A4}$$

Here, E is the mean entrainment velocity, W is the mesoscale vertical velocity (both in m s^{-1}), and γ is an empirical counteraction efficiency which controls the degree to which ascent offsets entrainment-driven ventilation. Combining these terms, we solve for the steady-state humidity:

$$q_{\mathrm{BL}} = \frac{\lambda q_s + \varepsilon_{\mathrm{eff}} q_{\mathrm{FT}}}{\lambda + \varepsilon_{\mathrm{eff}}}. \tag{A5}$$

A3 Isotopic Budget

The isotopic budget is solved for the isotopic ratio $R = \mathrm{D}/\mathrm{H}$. We enforce strict consistency between the mass fluxes defined above and the corresponding isotopic fluxes. Under steady-state conditions, the isotopic budget is written as

$$0 = F_{\mathrm{iso,E}} + F_{\mathrm{iso,ent}} + F_{\mathrm{iso,ex}}, \tag{A6}$$

where the terms represent surface evaporation, entrainment from the cloudy layer into the subcloud layer, and an effective cloud–rain isotopic exchange process, respectively. No additional export, dilution, or storage terms are included.

Isotopic ratios are converted to delta notation relative to VSMOW via

$$\delta = 1000\left(\frac{R}{R_{\mathrm{VSMOW}}} - 1\right), \tag{A7}$$

where R_{VSMOW} is the standard isotopic ratio.

A3.1 Consistent Craig–Gordon Evaporation

The isotopic evaporative flux is expressed as the product of the bulk mass flux and the isotopic ratio of the evaporating vapor, R_E:

$$F_{\mathrm{iso,E}} = F_E \cdot R_E. \tag{A8}$$

We adopt the linear-resistance form of the Craig–Gordon model (Craig and Gordon, 1965),

$$R_E = \frac{R_{\mathrm{oc}}/\alpha_{\mathrm{eq}} - \mathcal{H} R_{\mathrm{BL}}}{\alpha_k (1 - \mathcal{H})}, \tag{A9}$$

where R_{oc} is the ocean surface isotopic ratio, α_{eq} is the equilibrium fractionation factor at the sea surface temperature, α_k is the kinetic fractionation factor, and $\mathcal{H}$ is the near-surface relative humidity defined at the sea surface temperature.

Substituting the bulk flux expression $F_E = \lambda q_s (1 - \mathcal{H})$ into the isotopic flux formulation yields

$$F_{\mathrm{iso,E}} = [\lambda q_s (1 - \mathcal{H})] \cdot \left[\frac{R_{\mathrm{oc}}/\alpha_{\mathrm{eq}} - \mathcal{H} R_{\mathrm{BL}}}{\alpha_k (1 - \mathcal{H})}\right] = \frac{\lambda q_s}{\alpha_k}\left(\frac{R_{\mathrm{oc}}}{\alpha_{\mathrm{eq}}} - \mathcal{H} R_{\mathrm{BL}}\right), \tag{A10}$$

demonstrating explicit cancellation of the $(1 - \mathcal{H})$ dependence.

This formulation ensures that the isotopic flux is fully consistent with the mass budget and avoids artificial singular behavior as $\mathcal{H} \to 1$.

The evaporative isotopic flux is parameterized using a simplified Craig–Gordon framework that assumes a single effective kinetic fractionation factor and neglects explicit aerodynamic resistance terms. This formulation is intended to capture first-order isotopic effects under near-surface marine boundary layer conditions rather than to represent a complete microphysical description of evaporation.

A3.2 Entrainment and Exchange

The entrainment isotopic flux follows directly from the mass flux formulation,

$$F_{\mathrm{iso,ent}} = \varepsilon_{\mathrm{eff}} \left(q_{\mathrm{FT}} R_{\mathrm{FT}} - q_{\mathrm{BL}} R_{\mathrm{BL}} \right), \tag{A11}$$

where $\varepsilon_{\mathrm{eff}}$ is the effective entrainment velocity and subscripts FT and BL denote free-tropospheric and boundary-layer air, respectively.

We introduce an additional exchange term, $F_{\mathrm{iso,ex}}$, to parameterize isotopic equilibration between boundary-layer vapor and hydrometeors (cloud droplets or rain) during mesoscale ascent. This process is represented as a relaxation of boundary-layer vapor toward a target isotopic ratio R_{rain},

$$F_{\mathrm{iso,ex}} = k_{\mathrm{ex}} \, q_{\mathrm{BL}} \left(R_{\mathrm{rain}} - R_{\mathrm{BL}} \right). \tag{A12}$$

The exchange term $F_{\mathrm{iso,ex}}$ represents an effective parameterization of isotopic re-equilibration associated with precipitation and cloud processing, in which net vapor mass changes may be small even though isotopic exchange occurs through repeated phase changes. As such, this term modifies the isotopic composition of boundary-layer vapor without introducing an explicit moisture source or sink.

The exchange rate k_{ex} (s^{-1}) is parameterized as a bounded logistic function of mesoscale vertical velocity,

$$k_{\mathrm{ex}}(W) = \frac{k_{\mathrm{max}}}{1 + \exp(-W/w_{\mathrm{width}})}, \tag{A13}$$

reflecting the onset and intensification of cloud and precipitation processing during upward motion. The dependence of k_{ex} on W should therefore be interpreted as a proxy for cloud fraction and precipitation activity, rather than as a direct representation of a specific microphysical mechanism.

A4 Solution

Equation (A6) is linear in R_{BL}. Separating terms into sources (independent of R_{BL}) and sinks (proportional to R_{BL}):

$$\text{Source} = \frac{\lambda q_s}{\alpha_k \alpha_{\mathrm{eq}}} R_{\mathrm{oc}} + \varepsilon_{\mathrm{eff}} q_{\mathrm{FT}} R_{\mathrm{FT}} + k_{\mathrm{ex}} q_{\mathrm{BL}} R_{\mathrm{rain}}, \tag{A14}$$

$$\text{Sink Coeff.} = \frac{\lambda q_s \mathcal{H}}{\alpha_k} + \varepsilon_{\mathrm{eff}} q_{\mathrm{BL}} + k_{\mathrm{ex}} q_{\mathrm{BL}}. \tag{A15}$$

The steady-state ratio is $R_{\mathrm{BL}} = \text{Source}/\text{Sink Coeff.}$, which is converted to δ notation via $\delta_{\mathrm{BL}} = 1000(R_{\mathrm{BL}} - 1)$.

A5 Parameter Values

Parameters used in the standard run are listed below. Equilibrium fractionation α_{eq} is calculated following Majoube (1971), and the kinetic fractionation factor α_k is set to 1.0126 following Merlivat and Jouzel (1979) for the rough surface regime.

- **Environmental:** SST = 27.3°C, $p = 1013.25$ hPa, $h = 700$ m.
- **Coupling Timescale:** $\lambda = 1.16 \times 10^{-6}$ s^{-1} (corresponding to a surface moistening timescale of $\approx$ 10 days).
- **End Members:** $q_{\mathrm{FT}} = 13.0$ g kg^{-1}, $\delta_{\mathrm{FT}} = -90‰$, $\delta_{\mathrm{rain}} = -70‰$.
- **Entrainment Closure:** $\gamma = 0.30$.
- **Optimized Exchange:** $k_{\mathrm{max}} \approx 10^{-4}$ s^{-1}, $w_{\mathrm{width}} \approx 5.0$ mm s^{-1} (optimized within physically reasonable bounds).

We emphasize that this formulation is intended to demonstrate the existence of a physically plausible parameter regime capable of reproducing the observed contrast between humidity and isotopic gradients, rather than to identify a unique or optimal representation of boundary layer processes.

Author contributions. JG conceived the study, analyzed the data, developed the mixed-layer model, and wrote the manuscript. SL processed the isotopic data and contributed to the analysis. Both authors contributed to the interpretation and editing of the manuscript.

Competing interests. The authors declare no competing interests.

Acknowledgements. The authors used artificial intelligence (ChatGPT, OpenAI, 2025) to assist with coding the mixed-layer model and with drafting some initial text. All code, results, and manuscript content were thoroughly checked, validated, and revised by the authors, who take full responsibility for the accuracy and interpretation of the work. We acknowledge the EUREC4A campaign organizers and participants, particularly the crew of R/V Meteor and the HALO and P3 aircraft operations team. This work was supported by the U.S. National Science Foundation under grant AGS-1853353. We thank the German Research Foundation (DFG) for support of the EUREC^{4}A campaign under grant 264907654.

References

Albright, A. L., Bony, S., Stevens, B., and Vogel, R.: Observed subcloud-layer moisture and heat budgets in the trades, Journal of the Atmospheric Sciences, 79, 2363–2385, https://doi.org/10.1175/JAS-D-21-0337.1, 2022.

Bailey, A., Aemisegger, F., Villiger, L., Los, S. A., Reverdin, G., Galewsky, J., Noone, D., and Steen-Larsen, H. C.: Isotopic measurements in water vapor, precipitation, and seawater during EUREC^{4}A, Earth System Science Data, 15, 465–495, https://doi.org/10.5194/essd-15-465-2023, 2023.

Benetti, M., Aloisi, G., Reverdin, G., Risi, C., and Sèze, G.: Importance of boundary layer mixing for the isotopic composition of surface vapor over the subtropical North Atlantic Ocean, Journal of Geophysical Research: Atmospheres, 123, 2442–2461, https://doi.org/10.1002/2017JD027593, 2018.

Bony, S. and Dufresne, J.-L.: Marine boundary layer clouds at the heart of tropical cloud feedback uncertainties in climate models, Geophysical Research Letters, 32, L20 806, https://doi.org/10.1029/2005GL023851, 2005.

Bony, S. and Stevens, B.: Measuring area-averaged vertical motions with dropsondes, Journal of the Atmospheric Sciences, 76, 767–783, https://doi.org/10.1175/JAS-D-18-0141.1, 2019.

Bony, S., Stevens, B., Ament, F., Albright, A., Acquistapace, C., Aemisegger, F., Farrell, D., Galewsky, J., Giez, A., Lenschow, D., Nuijens, L., Rauber, R., Röttenbacher, J., Schnitt, S., Schulz, H., Vial, J., Winker, D., and Zhang, L.: EUREC^{4}A: A field campaign to elucidate the couplings between clouds, convection and circulation, Surveys in Geophysics, 38, 1529–1568, https://doi.org/10.1007/s10712-017-9428-0, 2017.

Bretherton, C. S. and Blossey, P. N.: Understanding Mesoscale Aggregation of Shallow Cumulus Convection Using Large-Eddy Simulation, Journal of Advances in Modeling Earth Systems, 9, 2798–2821, https://doi.org/10.1002/2017MS000981, 2017.

Craig, H. and Gordon, L. I.: Deuterium and oxygen-18 variations in the ocean and the marine atmosphere, in: Stable Isotopes in Oceanographic Studies and Paleotemperatures, edited by Tongiorgi, E., pp. 9–130, Consiglio Nazionale delle Ricerche, Laboratorio di Geologia Nucleare, Pisa, Italy, 1965.

Galewsky, J., Steen-Larsen, H. C., Field, R. D., Worden, J., Risi, C., and Schneider, M.: Stable isotopes in atmospheric water vapor and applications to the hydrologic cycle, Reviews of Geophysics, 54, 809–865, https://doi.org/10.1002/2015RG000512, 2016.

Galewsky, J., Jensen, M. P., and Delp, J.: Marine Boundary Layer Decoupling and the Stable Isotopic Composition of Water Vapor, Journal of Geophysical Research: Atmospheres, 127, e2021JD035 470, https://doi.org/10.1029/2021JD035470, 2022.

George, G., Stevens, B., Bony, S., Pincus, R., Fairall, C., Schulz, H., Kölling, T., Kalen, Q. T., Klingebiel, M., Konow, H., Lundry, A., Prange, M., and Radtke, J.: JOANNE: Joint dropsonde observations of the atmosphere in tropical North Atlantic meso-scale environments, Earth System Science Data, 13, 5253–5272, https://doi.org/10.5194/essd-13-5253-2021, 2021.

George, G., Stevens, B., Bony, S., Vogel, R., and Naumann, A. K.: Widespread shallow mesoscale circulations observed in the trades, Nature Geoscience, 16, 584–589, https://doi.org/10.1038/s41561-023-01215-1, 2023.

Janssens, M., Vilà-Guerau de Arellano, J., van Heerwaarden, C. C., de Roode, S. R., Siebesma, A. P., and Glassmeier, F.: Nonprecipitating Shallow Cumulus Convection Is Intrinsically Unstable to Length Scale Growth, Journal of the Atmospheric Sciences, 80, 849–870, https://doi.org/10.1175/JAS-D-22-0111.1, 2023.

Konow, H., Ewald, F., George, G., Jacob, M., Klingebiel, M., Kölling, T., Luebke, A. E., Mieslinger, T., Pörtge, V., Radtke, J., Schäfer, M., Schulz, H., Vogel, R., Wirth, M., Bony, S., Crewell, S., Ehrlich, A., Forster, L., Giez, A., Gödde, F., Groß, S., Gutleben, M., Hagen, M., Hirsch, L., Jansen, F., Lang, T., Mayer, B., Mech, M., Prange, M., Schnitt, S., Vial, J., Walbröl, A., Wendisch, M., Wolf, K., Zinner, T., Zöger, M., Ament, F., and Stevens, B.: EUREC^{4}A's HALO, Earth System Science Data, 13, 5545–5563, https://doi.org/10.5194/essd-13-5545-2021, 2021.

Lenschow, D. H., Krummel, P. B., and Siems, S. T.: Measuring Entrainment, Divergence, and Vorticity on the Mesoscale from Aircraft, Journal of Atmospheric and Oceanic Technology, 16, 1384–1400, https://doi.org/10.1175/1520-0426(1999)016<1384:MEDAVO>2.0.CO;2, 1999.

Lenschow, D. H., Savic-Jovcic, V., and Stevens, B.: Divergence and vorticity from aircraft air motion measurements, Journal of Atmospheric and Oceanic Technology, 24, 2062–2072, https://doi.org/10.1175/2007JTECHA940.1, 2007.

Lilly, D. K.: Models of cloud-topped mixed layers under a strong inversion, Quarterly Journal of the Royal Meteorological Society, 94, 292–309, https://doi.org/10.1002/qj.49709440106, 1968.

Majoube, M.: Fractionnement en oxygène 18 et en deutérium entre l'eau et sa vapeur, Journal de Chimie Physique, 68, 1423–1436, https://doi.org/10.1051/jcp/1971681423, 1971.

Merlivat, L. and Jouzel, J.: Global climatic interpretation of the deuterium-oxygen 18 relationship for precipitation, Journal of Geophysical Research: Oceans, 84, 5029–5033, https://doi.org/10.1029/JC084iC08p05029, 1979.

Pincus, R., Fairall, C. W., Bailey, A., Chuang, P., de Boer, G., Doyle, J., Fuchs, D., Galewsky, J., Ghate, V., Greatbatch, R., Greenslade, C., Grise, K., Haines, S., Haynes, J. M., Heffernan, J., Isarra, A., Knuth, F., Lundry, A., Nester, A., Noone, D., Pfister, L., Quinn, P. K., Rajib, Z., Richard, E., Royer, H., Schulz, H., Sorooshian, A., Speingys, N., Spangler, C., Sullivan, S., Tjernström, M., Turnbull, J., Wang, H., Witte, M. K., and Zuidema, P.: Observations from the NOAA P-3 aircraft during ATOMIC, Earth System Science Data, 13, 3281–3296, https://doi.org/10.5194/essd-13-3281-2021, 2021.

Radtke, J., Naumann, A. K., Hagen, M., and Ament, F.: The relationship between precipitation and its spatial pattern in the trades observed during EUREC^{4}A, Quarterly Journal of the Royal Meteorological Society, 148, 1913–1928, https://doi.org/10.1002/qj.4284, 2022.

Risi, C., Hourdin, F., Cattiaux, J., Steen-Larsen, H. C., Wong, C. S., Galewsky, J., Lacour, J.-L., Bonne, J.-L., Clerbaux, C., Coheur, P.-F., Hurtmans, D., and Worden, J.: The water isotopic version of the LMDZ general circulation model, Atmospheric Chemistry and Physics, 19, 12 235–12 263, https://doi.org/10.5194/acp-19-12235-2019, 2019.

Risi, C., Muller, C., and Blossey, P. N.: What Controls the Water Vapor Isotopic Composition Near the Surface of Tropical Oceans? Results from an Analytical Model Constrained by Large-Eddy Simulations, Journal of Advances in Modeling Earth Systems, 12, e2020MS002 106, https://doi.org/10.1029/2020MS002106, 2020.

Sherwood, S. C., Bony, S., and Dufresne, J.-L.: Spread in model climate sensitivity traced to atmospheric convective mixing, Nature, 505, 37–42, https://doi.org/10.1038/nature12829, 2014.

Stevens, B., Bony, S., Farrell, D., Ament, F., Blyth, A., Fairall, C., Karstensen, J., Quinn, P. K., Speich, S., Acquistapace, C., Aemisegger, F., Albright, A. L., Bellenger, H., Bodenschatz, E., Caesar, K.-A., Chewitt-Lucas, R., de Boer, G., Delanoë, J., Denby, L., Ewald, F., Fildier, B., Forde, M., George, G., Gross, S., Hagen, M., Hausold, A., Heywood, K. J., Hirsch, L., Jacob, M., Jansen, F., Kinne, S., Klocke, D., Kölling, T., Konow, H., Lothon, M., Mohr, W., Naumann, A. K., Nuijens, L., Olivier, L., Pincus, R., Pöhlker, M., Reverdin, G., Roberts, G., Schnitt, S., Schulz, H., Siebesma, A. P., Stephan, C. C., Sullivan, P., Touzé-Peiffer, L., Vial, J., Vogel, R., Zuidema, P., Alexander, N., Alves, L., Arixi, S., Asmath, H., Bagheri, G., Baier, K., Bailey, A., Baranowski, D., Baron, A., Barrau, S., Barrett, P. A., Batier, F., Behrendt, A., Bendinger, A., Beucher, F., Bigorre, S., Blades, E., Blossey, P., Bock, O., Böing, S., Bosser, P., Bourras, D., Bouruet-Aubertot, P., Bower, K., Branellec, P., Branger, H., Brennan, M., Brewer, A., Brilouet, P.-E., Brügmann, B., Buehler, S. A., Burke, E., Burton, R., Calmer, R., Canonici, J.-C., Carton, X., Cato Jr., G., Charles, J. A., Chazette, P., Chen, Y., Chilinski, M. T., Choularton, T., Chuang, P., Clarke, S., Coe, H., Cornet, C., Coutris, P., Couvreux, F., Crewell, S., Cronin, T., Cui, Z., Cuypers, Y., Daley, A., Damerell,

G. M., Dauhut, T., Deneke, H., Desbios, J.-P., Dörner, S., Donner, S., Douet, V., Drushka, K., Dütsch, M., Ehrlich, A., Emanuel, K., Emmanouilidis, A., Etienne, J.-C., Etienne-Leblanc, S., Faure, G., Feingold, G., Ferrero, L., Fix, A., Flamant, C., Flatau, P. J., Foltz, G. R., Forster, L., Furtuna, I., Gadian, A., Galewsky, J., Gallagher, M., Gallimore, P., Gaston, C., Gentemann, C., Geyskens, N., Giez, A., Gollop, J., Gouirand, I., Gourbeyre, C., de Graaf, D., de Groot, G. E., Grosz, R., Güttler, J., Gutleben, M., Hall, K., Harris, G., Helfer, K. C., Henze, D., Herbert, C., Holanda, B., Ibanez-Landeta, A., Intrieri, J., Iyer, S., Julien, F., Kalesse, H., Kazil, J., Kellman, A., Kidane, A. T., Kirchner, U., Klingebiel, M., Körner, M., Kremper, L. A., Kretzschmar, J., Krüger, O., Kumala, W., Kurz, A., L'Hégaret, P., Labaste, M., Lachlan-Cope, T., Laing, A., Landschützer, P., Lang, T., Lange, D., Lange, I., Laplacette, C., Lavik, G., Laxenaire, R., Le Bihan, C., Leandro, M., Lefevre, N., Lena, M., Lenschow, D., Li, Q., Lloyd, G., Los, S., Losi, N., Lovell, O., Luneau, C., Makuch, P., Malinowski, S., Manta, G., Marinou, E., Marsden, N., Masson, S., Maury, N., Mayer, B., Mayers-Als, M., Mazel, C., McGeary, W., McWilliams, J. C., Mech, M., Mehlmann, M., Meroni, A. N., Mieslinger, T., Minikin, A., Minnett, P., Möller, G., Morfa Avalos, Y., Muller, C., Musat, I., Napoli, A., Neuberger, A., Noisel, C., Noone, D., Nordsiek, F., Nowak, J. L., Oswald, L., Parker, D. J., Peck, C., Person, R., Philippi, M., Plueddemann, A., Pöhlker, C., Pörtge, V., Pöschl, U., Pologne, L., Posyniak, M., Prange, M., Quiñones Meléndez, E., Radtke, J., Ramage, K., Reimann, J., Renault, L., Reus, K., Reyes, A., Ribbe, J., Ringel, M., Ritschel, M., Rocha, C. B., Rochetin, N., Röttenbacher, J., Rollo, C., Royer, H., Sadoulet, P., Saffin, L., Sandiford, S., Sandu, I., Schäfer, M., Schemann, V., Schirmacher, I., Schlenczek, O., Schmidt, J., Schröder, M., Schwarzenboeck, A., Sealy, A., Senff, C. J., Serikov, I., Shohan, S., Siddle, E., Smirnov, A., Späth, F., Spooner, B., Stolla, M. K., Szkółka, W., de Szoeke, S. P., Tarot, S., Tetoni, E., Thompson, E., Thomson, J., Tomassini, L., Totems, J., Ubele, A. A., Villiger, L., von Arx, J., Wagner, T., Walther, A., Webber, B., Wendisch, M., Whitehall, S., Wiltshire, A., Wing, A. A., Wirth, M., Wiskandt, J., Wolf, K., Worbes, L., Wright, E., Wulfmeyer, V., Young, S., Zhang, C., Zhang, D., Ziemen, F., Zinner, T., and Zöger, M.: EUREC^{4}A: An Atlantic trade-wind cloud experiment, Earth System Science Data, 13, 4067–4119, https://doi.org/10.5194/essd-13-4067-2021, 2021.

Stull, R. B.: The energetics of entrainment across a density interface, Journal of the Atmospheric Sciences, 33, 1260–1267, https://doi.org/10.1175/1520-0469(1976)033<1260:TEOEAD>2.0.CO;2, 1976.

Touzé-Peiffer, L., Vogel, R., and Rochetin, N.: Cold pools observed during EUREC^{4}A: detection and characterization from atmospheric soundings, Journal of Applied Meteorology and Climatology, 61, 593–610, https://doi.org/10.1175/JAMC-D-21-0048.1, 2022.

Vogel, R., Albright, A. L., Vial, J., George, G., Stevens, B., and Bony, S.: Strong cloud–circulation coupling explains weak trade cumulus feedback, Nature, 612, 696–700, https://doi.org/10.1038/s41586-022-05364-y, 2022.